



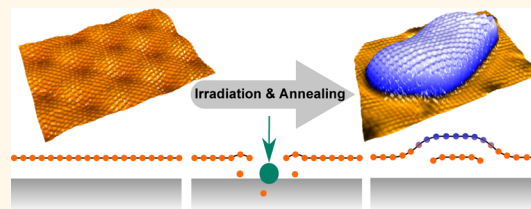
# Interfacial Carbon Nanoplatelet Formation by Ion Irradiation of Graphene on Iridium(111)

Charlotte Herbig,<sup>\*†</sup> E. Harriet Åhlgren,<sup>‡</sup> Wouter Jolie,<sup>†</sup> Carsten Busse,<sup>†</sup> Jani Kotakoski,<sup>‡§</sup> Arkady V. Krasheninnikov,<sup>⊥</sup> and Thomas Michely<sup>†</sup>

<sup>†</sup>II. Physikalisches Institut, Universität zu Köln, Zülpicher Straße 77, 50937 Köln, Germany, <sup>‡</sup>Department of Physics, University of Helsinki, Helsinki, Finland,

<sup>§</sup>Faculty of Physics, University of Vienna, Vienna, Austria, and <sup>⊥</sup>Department of Applied Physics, Aalto University, Helsinki, Finland

**ABSTRACT** We expose epitaxial graphene (Gr) on Ir(111) to low-energy noble gas ion irradiation and investigate by scanning tunneling microscopy and atomistic simulations the behavior of C atoms detached from Gr due to ion impacts. Consistent with our density functional theory calculations, upon annealing Gr nanoplatelets nucleate at the Gr/Ir(111) interface from trapped C atoms initially displaced with momentum toward the substrate. Making use of the nanoplatelet formation phenomenon, we measure the trapping yield as a function of ion energy and species and compare the values to those obtained using molecular dynamics simulations. Thereby, complementary to the sputtering yield, the trapping yield is established as a quantity characterizing the response of supported 2D materials to ion exposure. Our findings shed light on the microscopic mechanisms of defect production in supported 2D materials under ion irradiation and pave the way toward precise control of such systems by ion beam engineering.



**KEYWORDS:** graphene · ion irradiation · graphene nanoplatelets · trapping yield · STM · molecular dynamics · DFT

Triggered by their unique physical properties and low dimensionality, materials such as graphene (Gr), hexagonal boron nitride, and transition metal dichalcogenides were recently put into the limelight.<sup>1–5</sup> In order to meet application-oriented demands for these materials, one should be able to tailor their characteristics. Low-energy ion exposure combined with controlled thermal annealing is a versatile method to create defects and subsequently new morphologies in systems with reduced dimensionality.<sup>6,7</sup> Thus, obtaining quantitative information on ion-induced defects and their stability in two-dimensional (2D) systems is worthwhile, from both an applied and a fundamental point of view. Because in most practical applications, 2D materials are resting on a substrate, understanding the effect of the substrate on the defect production and annealing is mandatory for controlled ion beam processing and nanostructuring of 2D layers.

Previous experimental and theoretical work investigating ion beam exposure of supported Gr was focused on defect formation

and has already brought substantial new insights.<sup>8–16</sup> To name a few, Tapaszto *et al.*<sup>8</sup> as well as Ugeda *et al.*<sup>9,10</sup> characterized the effect of individual ion-induced point defects on the local electronic properties of Gr by scanning tunneling microscopy (STM). Buchowicz *et al.*<sup>11</sup> established a decreased electronic mobility as a consequence of ion-induced defect creation in Gr. Akcöltekin *et al.*<sup>12</sup> used swift heavy ions at grazing incidence to unzip Gr resting on a dielectric substrate. With the help of isotope labeling techniques, Kalbac *et al.*<sup>13</sup> found a substrate-assisted self-healing mechanism in the lower layer of supported bilayer Gr after ion exposure. Upon grazing incidence ion exposure Standop *et al.*<sup>14</sup> discovered interface channeling of ions between an Ir(111) substrate and Gr. On the basis of the analysis of damage annealing, they found re-bonding of dangling vacancy or vacancy cluster bonds with the substrate to give rise to the formation of an antidot lattice in Gr. Blanc *et al.*<sup>15</sup> used low-energy ion bombardment of Gr/Ir(111) to unravel the microscopic relationship between point defects

\* Address correspondence to herbig@ph2.uni-koeln.de.

Received for review July 15, 2014 and accepted December 8, 2014.

Published online December 08, 2014  
10.1021/nn503874n

© 2014 American Chemical Society

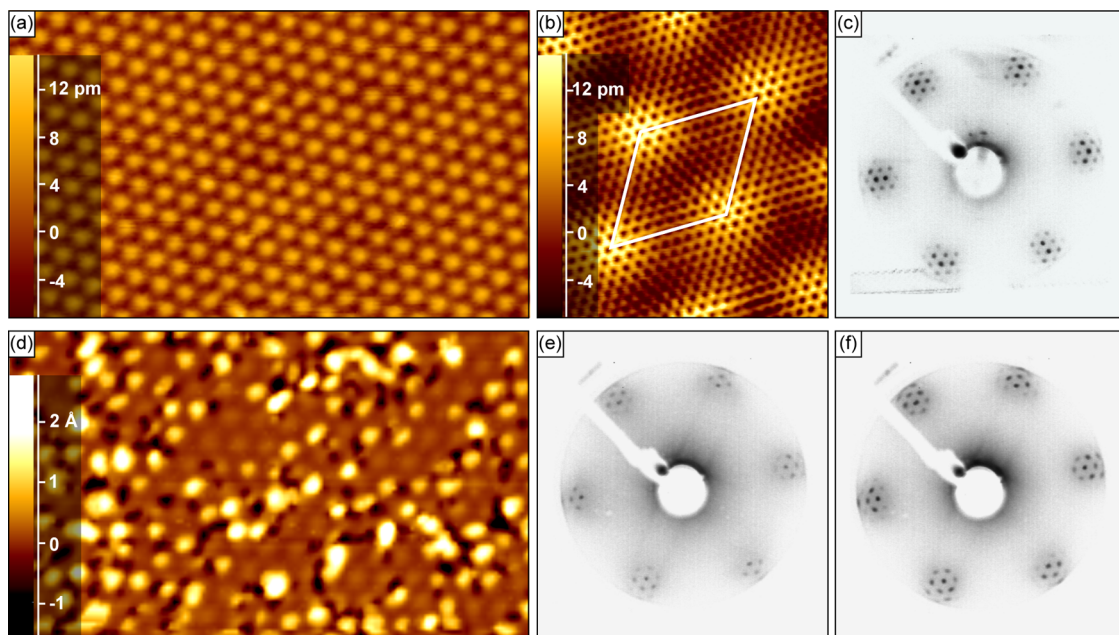


**Figure 1.** (a) STM topograph of Gr/Ir(111) prior to irradiation. The periodicity visible is the moiré superstructure. Image size is  $50 \text{ nm} \times 30 \text{ nm}$ . (b) Atomic resolution STM topograph of Gr/Ir(111). The moiré unit cell is indicated by white lines. Image size is  $6.6 \text{ nm} \times 6.9 \text{ nm}$ . (c) LEED pattern of the sample in (a) (electron energy is  $80 \text{ eV}$ , inverted contrast). (d) STM topograph of Gr/Ir(111) after exposure to  $F = 0.01 \text{ MLE}$  of  $1 \text{ keV Xe}^+$  ion irradiation at normal incidence and room temperature. Besides the moiré superstructure small protrusions and depressions are visible. Image size is  $50 \text{ nm} \times 30 \text{ nm}$ . (e, f) LEED patterns of the irradiated sample as shown in (d) before (e) and after (f) annealing to  $1000 \text{ K}$  (electron energy is  $80 \text{ eV}$ , inverted contrast). The diffuse background and the diffraction spot broadening due to irradiation in (e) largely vanishes upon annealing in (f), where the LEED pattern is comparable in quality to the pristine case (c).

and strain in epitaxial Gr. With the help of molecular dynamics (MD) simulations, Åhlgren *et al.*<sup>16</sup> found a pronounced difference between freestanding and supported Gr/Ir(111) for irradiation defect size and sputtering yield.

In the present work we focus on the fate of C atoms detached from Gr to gain a comprehensive picture of the impact events, an issue neglected so far. While for freestanding Gr, all removed C atoms leaving the layer in either forward or backward direction are sputtered, the situation differs considerably in the case of supported Gr. For supported layers, only atoms carrying backward momentum are sputtered, while the atoms carrying forward momentum are either trapped at the Gr/metal interface or implanted into the substrate.

Here, we show that by ion exposure and subsequent annealing Gr nanoplatelets form at the interface. On the basis of density functional theory (DFT) calculations, we conclude that these nanoplatelets represent all C atoms that were either implanted or detached and located at the interface to good approximation. A comparison between experimental and MD simulation results shows that the C atoms that end up in the nanoplatelets are detached from the Gr layer by the impinging low-energy ions with forward momentum. By measuring the area fraction of the nanoplatelets through STM, we obtain a new quantitative measure, the trapping yield, defined as the number of those detached C atoms per incident ion. It can be considered

as a complement to the sputtering yield for characterization of the ion–2D-layer interaction.

## RESULTS AND DISCUSSION

**Graphene Nanoplatelet Formation by Ion Irradiation and Annealing.** For reference, Figure 1a–c visualize an as-grown Gr layer on Ir(111). The height modulation in the STM topograph of Figure 1a reflects the moiré periodicity of  $2.53 \text{ nm}$  that results from the lattice mismatch between Gr [lattice parameter on Ir(111)<sup>17</sup>  $a_{\text{Gr}} = 2.452 \text{ \AA}$ ] and the Ir(111) surface lattice ( $a_{\text{Ir}} = 2.715 \text{ \AA}$ ). The atomic resolution STM topograph in Figure 1b displays the moiré unit cell with  $(10.32 \times 10.32)$  Gr unit cells resting on  $(9.32 \times 9.32)$  Ir(111) unit cells, with aligned dense-packed rows of Gr and Ir(111).<sup>17</sup> Due to the variation of the C atom positions with respect to the substrate, binding is inhomogeneous within the moiré cell. Gr is least strongly bound in the corners of the unit cell (top areas, bright in Figure 1b) and much stronger in the other two high-symmetry areas (named fcc and hcp areas). The Gr layer corrugation is  $\Delta h \approx 0.5 \text{ \AA}$ , and the average layer height is  $3.38 \text{ \AA}$ .<sup>18</sup> The corresponding low-energy electron diffraction (LEED) pattern in Figure 1c exhibits sharp first-order Ir and C spots surrounded by the moiré reflections.

After an ion fluence  $F = 0.01 \text{ MLE}$  of  $1 \text{ keV Xe}^+$ , a complex defect pattern emerges (see Figure 1d). Here, the ion fluence is measured in monolayer equivalents (MLE), with 1 MLE corresponding to the surface atomic

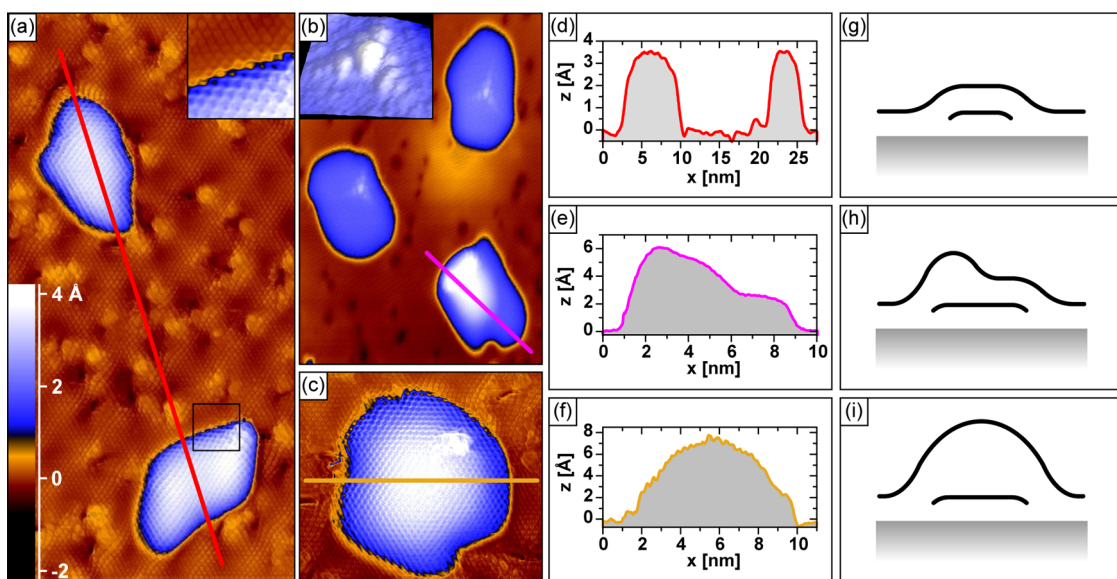


**Figure 2.** (a) Atomic resolution STM topograph of Gr/Ir(111) after 3 cycles of 0.01 MLE of 1 keV  $\text{Xe}^+$  normal incidence irradiation followed by annealing at 1000 K. Image size is  $16.5 \text{ nm} \times 29.7 \text{ nm}$ . Inset in upper right corner: Magnified view of the area indicated by the black square displaying a continuous Gr layer over the edge of a bulge. Color scale indicated in the lower left corner was chosen to make atomic resolution on the base level and on the nanoplatelets visible. Image size is  $2.6 \text{ nm} \times 2.5 \text{ nm}$ . (b) In the upper image part, two Gr bulges covering Gr nanoplatelets display a 3-fold symmetric ( $\sqrt{3} \times \sqrt{3}$ ) scattering pattern. In the lower part, a bulge is partly delaminated from the Gr nanoplatelet. See text. Image size is  $18.1 \text{ nm} \times 25.5 \text{ nm}$ . Inset in upper left corner: Magnified 3D view of a scattering pattern presented in (b). Image size is  $6 \text{ nm} \times 6 \text{ nm}$ . (c) Completely delaminated bulge. Image size is  $11.7 \text{ nm} \times 10.1 \text{ nm}$ . (d), (e), and (f) display height profiles along the lines indicated in (a), (b), and (c), respectively. (g), (h), and (i) are schematic cross sections corresponding to the height profiles in (d), (e), and (f), respectively.

density of Ir(111), *i.e.*,  $1.57 \times 10^{-19}$  particles per  $\text{m}^2$ . The moiré pattern is still visible in the undamaged areas, but the morphology is now dominated by dark depressions and bright protrusions. In a typical impact event, the ion penetrates the Gr layer, causes a collision cascade in the underlying Ir substrate, and gets stuck with a certain probability in the crystal. Through these processes C atoms are sputtered or displaced in the forward direction, and Ir bulk vacancies, surface vacancies, Ir adatoms on Ir(111), and clusters thereof are created. On the basis of previous work,<sup>14,16</sup> we interpret the dark depressions as vacancies or vacancy clusters in Gr, with their edge bonds bound to the Ir substrate and the bright protrusions as Ir adatoms at the interface. Since detached C atoms at the interface bind deep in 3-fold hollow sites (see below), it is unlikely that they give rise to protrusions comparable in height to the ones of the Ir adatoms. Likewise, also Ir surface vacancies under the Gr cover are probably invisible to STM. Due to the generated defects, after irradiation the LEED pattern depicted in Figure 1e displays a higher diffuse background intensity. Nevertheless, the persistent first-order Gr and Ir as well as the moiré reflections prove a largely intact Gr lattice. Annealing the damaged sample to 1000 K almost restores the initial LEED pattern and displays a similar low background and sharpness of reflections, as shown in Figure 1f.

The real space view of the residual damage after three cycles of 0.01 MLE of 1 keV  $\text{Xe}^+$  irradiation and

annealing to 1000 K is presented in Figure 2a through an atomic resolution STM topograph. Vacancy clusters (depressions) remain visible, but the small protrusions have disappeared. Instead, bulges with sizes extending over a few moiré unit cells are present. By detailed inspection (inset of Figure 2a) it becomes obvious that the Gr lattice rows are continuous over the edges of the bulges. The height profile displayed in Figure 2d along the red line in Figure 2a reveals a distinct bulge height of approximately  $3 \text{ \AA}$ .

We propose here that the bulges result from Gr nanoplatelets formed at the interface upon annealing under the Gr cover. The nanoplatelets incorporate those C atoms that were detached from the Gr sheet in the forward direction, *i.e.*, toward the substrate, thereby either being pushed to the interface (majority of atoms) or into the Ir bulk (no more than 2%, according to MD simulations, as described below). The proposed geometry is sketched in Figure 2g. The bulge height of  $\sim 3 \text{ \AA}$  is in good agreement with the graphite interlayer distance of  $3.36 \text{ \AA}$ .<sup>19</sup>

Strong support for the nanoplatelet interpretation can be found in Figure 2b. Often, we observe 3-fold symmetric scattering patterns on the bulges (magnified in the inset) that we interpret to be caused by residual ion induced point defect structures (*e.g.*, a monovacancy or a small cluster thereof). In scanning tunneling spectroscopy, we find the platelets to be decoupled from the Ir(111) substrate and that these scattering patterns display a strong peak in the local

density of states close to the Fermi level (compare Supporting Information Figures S1 and S2). The scattering patterns and the peaked density of states above the defects strikingly resemble the observations by Ugeda *et al.*<sup>20</sup> for monatomic C vacancies in a graphite lattice. The scattering patterns are observed only when Gr is well decoupled from the substrate. They are never observed for defects in Gr resting directly on Ir(111).

Additional support for our interpretation comes from the fact that the nanoplatelets ripen in a very similar fashion, as do small Gr islands on Ir(111)<sup>21</sup> (compare Supporting Information Figure S3). Moreover, the platelets attach to and grow into preexisting substrate steps, as is observed for small Gr islands on Ir(111)<sup>21</sup> (compare Supporting Information Figure S4).

We note that Gr growth at the interface between Ir(111) and a first Gr layer has already been reported by Nie *et al.*,<sup>22</sup> through deposition of atomic C or through segregation of C from the bulk of the Ir crystal. Here we can exclude nanoplatelet formation by segregation of C present in our crystal already prior to the experiment, since heating of the Gr-covered sample without irradiation even up to 1500 K never resulted in nanoplatelets or other indications for second layer Gr formation.

The bulges are *not* formed due to agglomeration of Ir adatoms to small Ir islands upon annealing. In previous work<sup>14</sup> we have demonstrated unambiguously that upon annealing Ir adatoms annihilate with Ir surface vacancies, resulting in a perfect Ir surface layer. Moreover, scanning tunneling spectroscopy (STS) on the bulges provides sound evidence that these areas are decoupled from the Ir metal (compare Supporting Information Figure S1).

We also rule out that the bulges are agglomerations of implanted noble gas atoms. Although noble gas is certainly implanted into the Ir crystal, trapped in bulk vacancies as well as bulk vacancy clusters, and partially released during annealing to 1000 K, the Gr cover will not protect it from desorption. Weakly bound Gr on Ir(111) rests about 3.4 Å above the Ir(111) substrate<sup>18</sup> and thereby provides ample space for noble gas diffusion. Noble gas atoms possess a low binding energy with desorption temperatures well below room temperature.<sup>23</sup> When incomplete Gr layers are irradiated, Gr platelets even form next to their edges (compare Supporting Information Figure S5). Gr platelets are firmly bound to the substrate and possess little driving force to escape from under the Gr sheet, while noble gas should be readily released through the edges. Note that even chemisorbed, strongly bound species intercalated between Gr and Ir(111) deintercalate well below 900 K.<sup>24,25</sup> Our interpretation does not conflict with room-temperature Ar trapping under a hexagonal boron nitride (h-BN) layer on Rh(111) as proposed by Cun *et al.*,<sup>26,27</sup> since h-BN is strongly bound to Rh(111),<sup>28</sup> thereby impeding the lateral mobility of implanted noble gas atoms.

The bulge in the lower part of Figure 2b together with the corresponding height profile depicted in Figure 2e reveals an additional interesting phenomenon: Some profiles partially exceed the typical height of 3 Å, indicating a partial delamination of the covering Gr layer. The proposed geometry is sketched in Figure 2h. Also complete delamination of the Gr cover is observed (see for example Figure 2c). A typical height for a delaminated bulge is approximately 8 Å (see Figure 2f and i).

One likely explanation for the delamination is based on the fact that Gr at room temperature is usually under compressive strain, as a result of its growth at high temperatures.<sup>29,30</sup> By delamination the arc length of Gr increases and thus compressive strain is released. In this picture delamination takes place above nanoplatelets, as the binding of the Gr cover to the platelets is presumably weaker than that to the Ir(111) substrate. N'Diaye *et al.*<sup>29</sup> found that the Gr bending energy required for delamination is part of the energy balance deciding whether strain or delamination prevails. Only the largest bulges delaminate, since the energy penalty for bending is lower, the smaller the bending curvature is. Also the growth of a second Gr layer on an existing nanoplatelet cannot be excluded, for instance assisted by a defect. Such a growth by segregation of a second layer underneath Gr on Ir(111) has in fact been observed by Nie *et al.*<sup>22</sup> However, since C is supplied toward the edge of the nanoplatelet where incorporation into the existing platelet is facile, and considering the nucleation barrier that has to be surmounted for platelet formation (see below), this scenario appears to be less likely.

**Energetics of Nanoplatelet Formation from *ab Initio* Calculations.** To get microscopic insight into the nanoplatelet formation process, using *ab initio* calculations, we studied the energetics of monomers, dimers, and small C platelets in and on Ir with and without a Gr layer on top. As we show below, the energetics of C atoms on the free Ir(111) surface and at the interface with a Gr layer is similar, so we carried out most calculations for the free surface, which allowed us to avoid excessive computations.

The energy of formation per atom,  $E_c(N)$ , for a platelet consisting of  $N$  C atoms on a surface of a metal slab is defined as

$$E_c(N) = (E_{\text{tot}}[\text{slab} + N] - E_{\text{tot}}[\text{slab}]) / N - \mu_G \quad (1)$$

where  $E_{\text{tot}}[\text{slab} + N]$  and  $E_{\text{tot}}[\text{slab}]$  are the total energies of the slab with and without the adsorbed  $N$ -atom graphene platelet, respectively, and  $\mu_G$  is the chemical potential of a C atom in free-standing Gr.  $E_c(N)$  can be interpreted as the energy penalty per C atom to form an  $N$ -atom platelet on the metal with respect to an infinite Gr sheet. Note that for  $N \rightarrow \infty$ ,  $E_c$  gives the van der Waals Gr–metal interaction energy (per C atom), which is essentially zero as compared to typical values

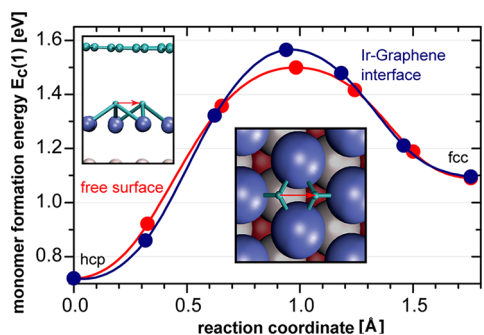


**Figure 3.** Variation of monomer formation energy  $E_c(1)$  along the minimum energy path from an hcp to an fcc adsorption site during the migration of a C-monomer on Ir(111) (red) and at the interface of Gr/Ir(111) (blue). The insets show the atomic geometries of the C-monomer in the hcp and the fcc 3-fold hollow sites as well as the migration path. The points are the results of nudged elastic band DFT calculations. Lines are to guide the eye.

of  $E_c$  for small platelets.  $E_c(1)$  is the C-monomer formation energy. Adding the cohesive energy of Gr to  $E_c(1)$  yields the C-monomer binding energy to the slab. The interstitial formation energy is given by

$$E_c(\text{int}) = (E_{\text{tot}}[\text{slab} + \text{int}] - E_{\text{tot}}[\text{slab}]) - \mu_G \quad (2)$$

where  $E_{\text{tot}}[\text{slab} + \text{int}]$  is the total energy of the slab including the interstitial.

First, we assessed the solubility of C atoms in Ir. The C interstitial formation energy,  $E_c(\text{int})$ , in bulk Ir is 2.56 eV in the octahedral and 3.32 eV in the tetrahedral configuration. Therefore, the equilibrium concentration of C atoms in bulk Ir at 1000 K is negligible, even taking into account the vibrational and electronic entropy contributions.

For C-monomers on Ir(111), we found that the most favorable adsorption position is the hcp 3-fold hollow site with  $E_c(1) = 0.72$  eV (see Figure 3). The C-monomer is located about 1 Å above the Ir surface. At the fcc 3-fold hollow site  $E_c(1) = 1.08$  eV; that is, adsorption at this site is disfavored by 0.36 eV. Since both values for  $E_c(1)$  are considerably lower than  $E_c(\text{int})$ , C atoms implanted into the Ir underneath the Ir(111) surface layer will have a strong tendency to segregate to the surface upon annealing.

Next, we analyzed the adsorption of C-monomers on Gr. Compared to adsorption on Ir(111), it is disfavored by nearly 6 eV. Thus, monomers detached from Gr by the ion impact and pushed to the interface will bind to Ir(111) and not to Gr. This decreases the probability for the reincorporation of detached C atoms into the Gr lattice, leaving the C atoms available for nanoplatelet formation at the interface. We note that the most probable route for C atoms trapped between Gr and Ir to be incorporated back into the Gr atomic network is through the annihilation with a vacancy attached to the Ir surface, *cf.* Figure 3 in ref 14. Our calculations indicate that at least for some configurations there is a potential energy barrier of several electronvolts hindering this process.

We also calculated the activation energy for C-monomer diffusion in Ir bulk and on Ir(111) using the nudged elastic band (NEB) method.<sup>31</sup> With activation energies of 1.6 eV in the bulk and 0.8 eV on the surface, C-monomers are highly mobile at the annealing temperature. They easily segregate to the surface and migrate on it. Calculations for the monomer at the Gr/Ir(111) interface resulted in similar numbers. In the top areas of the moiré, the C-monomer formation energy at the interface of Gr/Ir(111) is almost identical to the one on bare Ir(111), while in the fcc and hcp areas it is disfavored by 0.2 eV as compared to bare Ir(111). The migration barrier at the interface of Gr/Ir(111) is only marginally increased compared to the one on bare Ir(111), as obvious from Figure 3.

To understand the energetics of nanoplatelet formation, we calculated  $E_c(N)$  in small platelets of C atoms in  $\text{sp}^2$ -hybridized configurations on Ir(111) (red data in Figure 4).  $E_c(N)$  first increases; that is, the formation of dimers and small C platelets is energetically unfavorable with regard to spatially separated monomers. Such a behavior of C-monomers, which is at variance with that on copper,<sup>32</sup> originates from the large separation between the hcp and fcc sites on Ir(111) as compared to the carbon dimer bond length (1.6 Å vs 1.2 Å). Consequently, the dimer is "stretched" when the two C atoms are put in the neighboring lowest energy hcp and fcc positions. The trend is reversed when the platelets become larger; that is, then  $E_c(N)$  decreases with platelet size. The critical size is 5 atoms and the nucleation barrier is about 3 eV (~0.6 eV per atom).

Ion-induced surface damage of the Ir substrate consists in surface vacancies and Ir adatoms. Also clusters of both types of point defects are already present after room-temperature ion exposure. They coarsen and gain in size during the initial annealing stages, until eventually adatoms recombine with surface vacancies and the Ir surface damage is largely healed at 750 K.<sup>14</sup> To mimic the effect of this surface damage during the initial stages of annealing, we also calculated formation energies of small platelets at an Ir step edge, which might be considered as the boundary of an adatom or surface vacancy cluster. As seen from the blue data in Figure 4, the nucleation barrier decreases by about 2 eV due to the presence of the step, while the size of the critical nucleus remains unchanged. Therefore, we conclude that the presence of Ir damage during the initial stages of annealing will assist nanoplatelet formation by lowering the nucleation barrier. The relevance of substrate step edges (or cluster boundary edges) for Gr nanoplatelet formation is in perfect agreement with previous observations for the preferential growth of Gr islands at steps.<sup>21</sup> During annealing, nanoplatelets formed at the Gr/Ir(111) interface ripen, as do small Gr flakes on Ir(111) resulting from room-temperature C deposition in the absence of

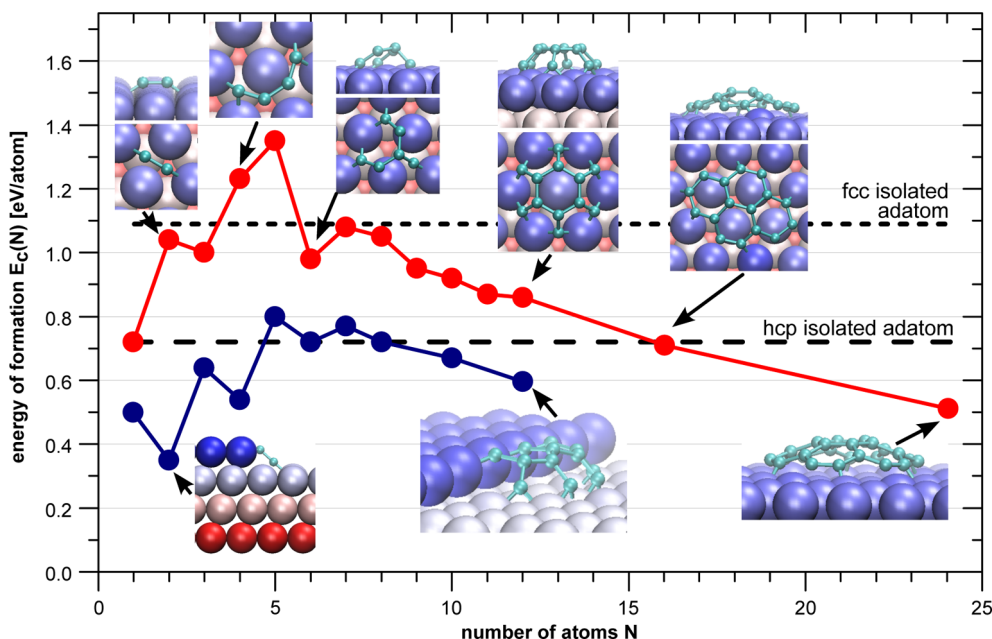


**Figure 4.** Energy of formation  $E_c(N)$  per atom (with regard to the energy of a C atom in an isolated infinite graphene sheet) in platelets consisting of  $N$  atoms on the Ir(111) terrace (red data) and at the step edge (blue data) as calculated by DFT. Lines are to guide the eye. The insets show some platelet configurations. Ir atoms represented as large balls are colored according to their z-coordinate. The nucleation barrier is smaller for platelets attached to the step edge.

ion irradiation.<sup>21</sup> To visualize ripening, an annealing sequence of an ion-irradiated Gr/Ir(111) sample is presented in the Supporting Information. We note that at room temperature nanoplatelets are immobile, as confirmed by STM.

In summary, our DFT calculations are consistent with the view that the C atoms, detached with forward momentum by ion impacts, agglomerate to graphene nanoplatelets at the Gr/Ir(111) interface upon annealing to 1000 K. The ion-induced damage in the Ir substrate assists nanoplatelet formation by lowering the nucleation barrier for it.

**Trapping Yield: Dependence on Ion Energy and Mass.** We are now ready to exploit the fact that the nanoplatelet area represents the C atoms detached from Gr with forward momentum. We will use the estimated number of C atoms in the nanoplatelets, normalized to the ion fluence, as experimental trapping yield,  $Y_t$ . Below, we investigate by STM and MD simulations how  $Y_t$  varies with projectile energy as well as its species and, thereby, elucidate the origin of these variations.

We start with an analysis of the ion energy dependency of the irradiated and annealed morphology, using  $Xe^+$  as ion species, a fixed fluence of  $F = 0.03$  MLE, and 1000 K as annealing temperature. Figure 5a–e display equally sized STM topographs after exposure and annealing in the energy range from 0.1 to 5 keV. All topographs exhibit bulges covering nanoplatelets and also a certain fraction of delaminated bulges. The nanoplatelet size tends to shrink with increasing ion energy, while the number density of the nanoplatelets increases. Exact numbers on mean platelet size and

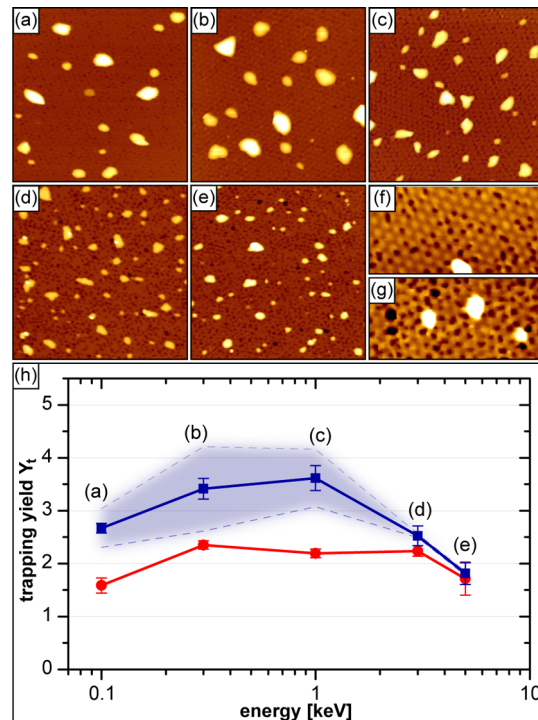


**Figure 5.** Dependence of trapping yield on ion energy: STM topographs of Gr/Ir(111) after  $Xe^+$  ion irradiation under normal incidence with increasing energies of (a) 0.1 keV, (b) 0.3 keV, (c) 1 keV, (d) 3 keV, and (e) 5 keV, fluence  $F = 0.03$  MLE, and  $T_{\text{anneal}} = 1000$  K. All image sizes are  $80 \text{ nm} \times 80 \text{ nm}$ . (f, g) Close-up of (a) and (e), respectively. Image sizes are  $40 \text{ nm} \times 20 \text{ nm}$ . (h) Trapping yield,  $Y_t$ : experimental (solid blue squares) and MD data (red dots) with the standard error of the mean plotted against projectile energy  $E$ . Blue-shaded area indicates experimental uncertainty due to delaminated bulges (see text).

number density with respect to ion energy are provided as Supporting Information. Within the energy range chosen, the larger the ion energy, the more severe the surface damage in the underlying Ir substrate.<sup>33,34</sup> Knowing from our DFT calculations that the Ir surface damage assists nanoplatelet formation, it is no surprise that at higher ion energies the number density of nanoplatelets increases. As visible in the magnified view of Figure 5f, small vacancy clusters located within the fcc and hcp areas of the moiré are already visible for the lowest ion energy. They reflect the limited mobility of vacancies in Gr on Ir(111) and the energetically strongly preferred rebonding of Gr dangling bonds to the substrate in these areas, as discussed by Standop *et al.*<sup>14</sup> Only for energies of  $\geq 3$  keV, larger vacancy clusters are apparent, as exemplified by the magnified view in Figure 5g after 5 keV Xe<sup>+</sup> irradiation. The increased carbon sputtering may be traced back to a more violent cascade in the Ir substrate, causing a higher probability of recoil Ir atoms hitting the Gr layer from below, resulting in sputtering of C atoms from the Gr.

The trapping yield,  $Y_t$ , estimated by STM image analysis is plotted in Figure 5h as a function of Xe<sup>+</sup> ion energy. While the trend of  $Y_t$  with ion energy does not depend on the details of our analysis procedure described in the Methods section, considerable uncertainty is introduced by the delaminated bulges, for which the size of the Gr nanoplatelets underneath cannot be determined. The blue data points plotted in Figure 5h assume for the delaminated bulges only half the area to be filled by nanoplatelets. The robustness of our analysis is documented by the boundaries of the blue-shaded area, which assume filling by either 25% or 75% with nanoplatelets, but still display the same trend of the data. As obvious from Figure 5h,  $Y_t$  increases from 0.1 to 0.3 keV, reaches a maximum in the range of 0.3 to 1.0 keV, and then drops again.

On the basis of mass conservation the trapping yield ( $Y_t$ ) of C atoms detached in the forward direction, the sputtering yield ( $Y_s$ ) of C atoms that left the sample in the backward direction, and the vacancy yield ( $Y_v$ ) of atoms missing in the initial graphene sheet are related:  $Y_s = Y_v - Y_t$ . Thus, a determination of the missing Gr atoms in the initial Gr sheet would be highly desirable and allow one also to access experimentally  $Y_s$ . However, such an attempt encounters difficulties that even impede obtaining the trend of  $Y_s$  with energy or other parameters. (i) On the basis of preliminary MD simulations,  $Y_s$  is up to a factor of 5 lower than the calculated  $Y_t$  and becomes comparable in magnitude only for the highest ion energies and heaviest species calculated. Subtracting two large quantities, of which at least one has a large error, results in amplification of the relative error of the desired quantity. (ii) Possibly an even more serious hindrance is the experimental fact that even after annealing to 1000 K the C atoms removed from

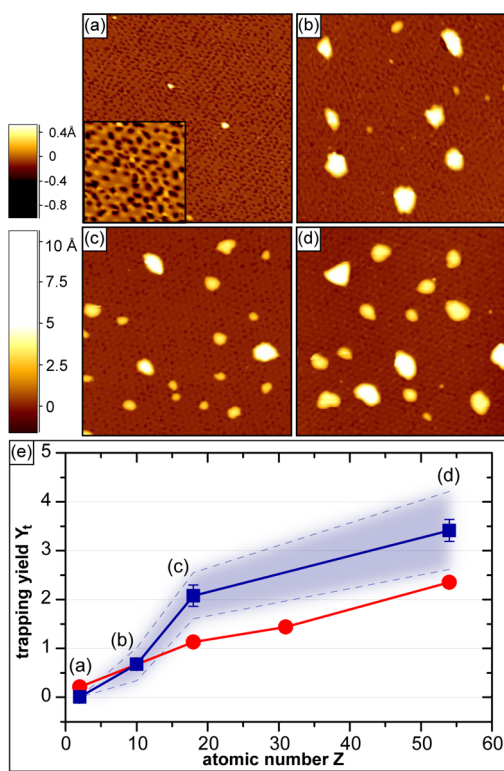
the initial Gr sheet are still largely represented by small vacancy clusters pinned to the preferential binding sites in each moiré unit cell. The size of these clusters cannot be determined even by atomic resolution STM (compare also ref 14), since their edges bend down to the substrate. On the basis of the number density of the small vacancy clusters measured, we just can note that an average cluster size of 4–10 vacancies would already account for the material trapped. Thus, experimental determination of  $Y_v$  is, under these conditions, next to impossible, and only dedicated experiments might bring a solution. In future work it will be explored whether sputtering at very high temperature, where the vacancy clusters detach from the moiré unit cells, results in large vacancy islands, of which the area can be determined with reasonable accuracy.

Direct estimation of the trapping yield ( $Y_t$ ) from the MD simulations is somewhat hampered by the limited time scales accessible within the simulations. A detailed description regarding the definition of the trapping yield from our MD results is given in the Methods section. Qualitatively, the MD simulations display the same energy dependence, but the absolute numbers are somewhat lower. They show that at low energies the ion impacts result only in a modest momentum transfer to the C atoms, in many cases insufficient to detach them from Gr and thus to transfer them to the Ir substrate for nanoplatelet formation. At high energies, the scattering cross section for the collision of the primary ion with a C atom decreases. Therefore, in fewer cases the ion directly detaches a C atom in the forward direction. Consequently, the trade-off between momentum transfer (favored by increasing ion energy) and scattering cross section (shrinking with increasing ion energy) implies a maximum in the trapping yield at intermediate energies. This behavior is similar to the forward-sputtering yield for free-standing Gr,<sup>35</sup> although the maximum is slightly shifted toward higher energies.

Since the scattering cross section and with it the trapping yield should scale with the atomic number of the projectile, we next turn to the investigation of the dependence of  $Y_t$  on the ion species at normal ion incidence. We exposed a complete Gr layer to the noble gas species with atomic numbers  $Z = 2, 10, 18$ , and 54 and conducted three cycles of ion exposure and annealing with total fluences of  $F = 0.3$  MLE, 0.1 MLE, 0.03 MLE, and 0.03 MLE, respectively. The data set is shown in Figure 6a–d with the corresponding plot in Figure 6e representing  $Y_t$  with respect to the atomic number  $Z$ .

Comparing the STM topographs in Figure 6a–d, it can indeed be recognized that trapping strongly increases with atomic number. This increase is even stronger than visually represented by the topographs, since the fluences for He<sup>+</sup> (Figure 6a) and Ne<sup>+</sup> (Figure 6b) are 10 and 3 times higher than the fluence

for  $\text{Ar}^+$  (Figure 6c) and  $\text{Xe}^+$  (Figure 6d) irradiation. The quantitative analysis of the experiments shown in



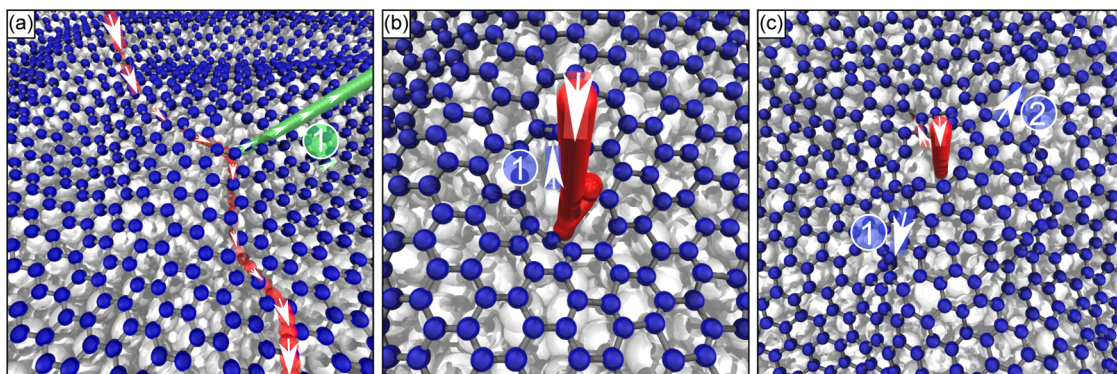
**Figure 6.** STM topographs of Gr/Ir(111) after three cycles of 0.3 keV normal incidence ion irradiation and annealing to 1000 K. Projectile atomic number and total ion fluence are (a) 2 ( $\text{He}^+$ ),  $F = 0.3 \text{ MLE}$ , (b) 10 ( $\text{Ne}^+$ ),  $F = 0.1 \text{ MLE}$ , (c) 18 ( $\text{Ar}^+$ ),  $F = 0.03 \text{ MLE}$ , and (d) 54 ( $\text{Xe}^+$ ),  $F = 0.03 \text{ MLE}$ . Image sizes are  $80 \text{ nm} \times 80 \text{ nm}$ . Inset in (a) is  $20 \text{ nm} \times 20 \text{ nm}$ . Lower color scale corresponds to (a)–(d); upper color scale to inset in (a). (e) Experimental (solid blue squares) and MD values (red dots) for  $\gamma_t$  plotted against atomic number  $Z$ . Blue-shaded area indicates experimental uncertainty due to delaminated bulges as for Figure 5h.

Figure 6e (full squares) is well reproduced by the results of the corresponding MD simulations (dots).

Interestingly, as visible from the inset in Figure 6a, for  $\text{He}^+$  irradiation we find almost no C trapping at the interface, but a substantial amount of vacancies in the covering Gr layer, *i.e.*, significant C atom sputtering. In view of practical application, this behavior opens a route toward the realization of a Gr nanomesh<sup>14</sup> fabricated on a metal substrate without trapping.

Additional insight is obtained by an analysis of individual MD simulation events. We start with the discussion of a characteristic 0.3 keV  $\text{He}^+$  event displayed in Figure 7a 0.6 ps after the impact. The impinging ion penetrates the Gr layer without damage and is then reflected at the metal substrate. Upon further reflection at the Gr sheet, it sputters one C atom toward the vacuum (see Supporting Information for a movie of the event). After backscattering at the Gr sheet, the ion is again reflected at the substrate, moves through the Gr, and escapes into the vacuum. In other simulation events, sputtering is caused by a displaced carbon atom instead of the ion itself. The combination of normal incidence transparency of Gr for He, the high backscattering probability of He at Ir with little energy loss due to the mass ratio 4:192, and the lower Gr transparency for backscattered He or carbon atoms arriving from the backside at off-normal, often grazing, incidence give rise to the comparatively high sputtering yield of He, combined with low trapping.

It is instructive to oppose the 0.3 keV  $\text{He}^+$  event with a typical 0.3 keV  $\text{Xe}^+$  event, as displayed in Figure 7b 0.6 ps after the ion impact. Unlike He, 0.3 keV Xe ions cannot go through Gr without displacing C atoms. On its way forward, the Xe ion disrupts the Gr layer, detaches a C atom entirely from Gr, and comes to rest almost instantaneously upon encounter with the Ir



**Figure 7.** Top view representations of MD snapshots after single-ion impacts at normal incidence. (a) Frame of a 0.3 keV He irradiation event at 598 fs with overlaid intermediate positions of the ion (red) and a sputtered C atom (green, marked by white number on green background). The ion first penetrates Gr without damage, is then reflected at the Ir substrate, and sputters upon further reflection at the Gr sheet one carbon toward the vacuum. The ion undergoes a second reflection at the substrate before it moves through the Gr sheet and escapes to the vacuum. (b) Frame of a 0.3 keV Xe irradiation event at 579 fs. The ion impacts the Gr sheet, pushing it toward the substrate and detaching one C atom, which becomes trapped (marked with the arrow and number on a blue background). (c) Frame for a Xe irradiation event at 5 keV after 398 fs with intermediate ion positions overlaid (red). The ion impacts the Gr sheet, detaching two C atoms, which get significant momenta in the in-plane direction before becoming trapped (marked with arrows and numbers on blue background). Complete movies of the events are provided as Supporting Information (He-0.3 keV.avi, Xe-0.3 keV.avi, and Xe-5.0 keV-0.avi, respectively).

substrate, due to efficient energy transfer (mass ratio 131:192). No sputtering takes place, and besides the detached C atom (marked with an arrow on blue background in Figure 7b) several additional under-coordinated C atoms adhere to the substrate and might become trapped during annealing. Thus, the substantial trapping for this Xe event, opposed to the He one displayed in Figure 7a, is consistent with the average displayed in Figure 6e.

Comparing the 0.3 keV  $\text{Xe}^+$  event of Figure 7b to a 5 keV  $\text{Xe}^+$  event as shown in Figure 7c illuminates the effect of ion energy on the trapping mechanism. For this event, the ion impacts close enough to the C atoms in Gr to account for the decreased cross section. Rather than pushing the Gr sheet forward toward the substrate, the ion displaces C atoms in the in-plane direction. For the example presented in Figure 7c two displaced C atoms get trapped a few lattice sites away from the impact point. Also here, several additional under-coordinated C atoms adhere to the substrate and might become trapped during annealing.

Finally, we note that changing the angle of incidence of the primary ion changes the balance of sputtering and trapping. Ions impinging under grazing incidence (e.g., 75°) display a C sputtering yield enhanced by about an order of magnitude compared to normal incidence (compare Standop *et al.*<sup>14</sup>). The origin of the enhanced sputtering is the channeling

effect, which causes the primary ion to repetitively hit Gr from below, whereby C atoms are displaced toward the vacuum. Consequently, trapping is comparatively diminished.

## CONCLUSION

In conclusion, through STM experiments and atomistic simulations we show that C atoms detached from supported Gr on Ir(111) with forward momentum are trapped and form upon annealing—assisted by irradiation-induced defects in the Ir substrate—nanometer-sized Gr nanoplatelets at the interface. The incorporation of detached C atoms into the Gr layer is suppressed due to the high affinity of C atoms to Ir(111), while diffusion into the Ir substrate is energetically unfavorable. By measuring the area fraction of the nanoplatelets, we establish the trapping yield ( $Y_t$ ) as an observable, defined as the number of trapped C atoms per incident ion. We detect a maximum in  $Y_t$  for energies around 0.3–1.0 keV and reveal an increase of  $Y_t$  with increasing projectile atomic number.  $\text{He}^+$  irradiation turned out to be a suitable tool to create vacancies within the Gr layer without considerable nanoplatelet formation at the interface. Our findings shed light on the atomic-scale mechanisms in operation during ion irradiation of metal-supported Gr and are a step toward precise ion beam manipulation of supported 2D layers.

## METHODS

Experiments are performed in an ultra-high-vacuum STM system with a base pressure below  $3 \times 10^{-11}$  mbar. The Ir(111) substrate is prepared by cycles of 2 keV noble gas ion irradiation at room temperature and at 970 K followed by annealing to 1520 K. A high-quality, fully closed Gr layer is then grown by room-temperature adsorption of ethylene, thermal decomposition at 1470 K, and subsequent dosing of  $4 \times 10^{-8}$  mbar of ethylene at 1270 K for 360 s. Ion irradiation is performed at room temperature with  $\text{He}^+$ ,  $\text{Ne}^+$ ,  $\text{Ar}^+$ , and  $\text{Xe}^+$  in the energy range from 100 eV to 5 keV perpendicular to the surface. Prior to each experiment, the ion flux is measured by a Faraday cup.

As damage accumulation can affect defect production in Gr,<sup>36</sup> we established experimental conditions such that the probability of an ion impinging on a damaged Gr area remains small. This was accomplished by ion irradiation in consecutive cycles of low fluence irradiation and annealing. If not stated otherwise, we implemented for each parameter set (ion energy and mass) three cycles with an ion fluence of  $F = 0.01$  MLE and annealing temperature of 1000 K for 300 s.

Subsequently, the surface is imaged by STM at room temperature. Typical tunneling parameters are  $U_s \approx -1$  V for the sample bias and  $I_t \approx 1$  nA for the tunneling current. For global structural characterization, additional LEED patterns were recorded and are presented with inverted contrast for better visibility.

To quantify  $Y_t$ , the area fraction of Gr nanoplatelets at the interface is estimated. The Gr cover layer bulges above the nanoplatelets to a typical height around 3 Å, when the bulge adheres to the nanoplatelet. However, the largest ones often do not adhere, and heights up to 10 Å are measured. The nanoplatelet size under these delaminated bulges is uncertain and may be substantially smaller than the bulge area. Therefore, we measured the total bulge area and the area of the delaminated

bulges separately. This was accomplished by setting two thresholds, one of 2.1 Å and one of 3.9 Å above the Gr base level. The area  $A_{2.1\text{\AA}}$  above the first threshold was taken as total bulge area; the area  $A_{3.9\text{\AA}}$  above the second threshold as the area of the delaminated bulges. To obtain a measure for  $Y_t$ , we subtracted a fraction  $x = 0.5$  of  $A_{3.9\text{\AA}}$  from  $A_{2.1\text{\AA}}$  but represented also the data with  $x = 0.25$  and  $x = 0.75$  in the figures in order to visualize the robustness of our approach for obtaining the trends of  $Y_t$  with ion energy and mass.

The first-principles DFT calculations were performed using the plane-wave-basis-set Vienna *ab initio* simulation package.<sup>37,38</sup> The projector augmented wave approach<sup>39</sup> was used to describe the core electrons, and a nonlocal van der Waals functional<sup>40</sup> to describe exchange and correlation. A plane wave kinetic energy cutoff of 400 eV was found to converge energy differences between different configurations within 0.1 eV. The same accuracy was achieved with regard to the number of k-points ( $3 \times 3 \times 1$ ) in the two-dimensional Brillouin zone. All structures were relaxed until atomic forces were below 0.002 eV/Å. The calculations were carried out for a 200-atom  $10 \times 10$  Gr supercell on top of a  $9 \times 9$  three-atomic-layer-thick Ir(111) slab containing 243 atoms, as in our previous work,<sup>14,15</sup> or for the same Ir slab without Gr. Besides, to assess the role of Ir atoms in the nanoplatelet formation process, we also carried out simulations for a rectangular 272-atom Ir slab with a step on the (111) surface. Vacuum of 20 Å was added in the transverse direction to separate the periodic images of the slab.

For the classical MD calculations we used the PARCAS code.<sup>41</sup> Our MD simulation cell included 45 900 substrate atoms and 2584 C atoms set on top of the substrate at a distance of 3.31 Å. For the two subsystems to coincide, we stretched the substrate lattice constant for 1% from the relaxed value. To model the substrate, we used Pt atoms instead of Ir atoms, because a well-established interaction model exists for Pt–Pt

and Pt–C<sup>42</sup> unlike for Ir–Ir and Ir–C. Due to the similarity in atomic masses, structure, and chemistry of these two atomic species, only minor differences at the analytical potential level of description can be expected in the simulation results. The C–C interactions were modeled using a bond-order potential by Brenner *et al.*<sup>43</sup> with a repulsive part<sup>44</sup> for small atom separations and the ion interactions by the universal repulsive potential.<sup>44</sup> The charge state of the ion was not considered in the simulations because the ion energies were low and energy transfer from the ion to the target atoms was fully nuclear in nature. For each simulation, one ion was shot toward the system at a randomly chosen impact point, after which the system was allowed to relax prior to analysis. Approximately 300 impact points were selected for each ion-energy pair. The simulation time was set to 0.5 ns at 0 K with heat dissipation at the edges of the system modeled with the Berendsen thermostat.<sup>45</sup> The trapping yield was estimated by calculating the number of C atoms detached from the Gr sheet in the direction of the substrate. In general, only a small fraction of the detached atoms (less than 2% for all studied ions and energies) were embedded into the substrate due to irradiation, whereas many more atoms were displaced to the Gr–Ir interface or remained partially bound to the Gr sheet. We found that a good description for the trapping yield can be obtained by counting all carbon atoms detached from the Gr sheet either into the substrate or into the interface area plus undercoordinated C atoms remaining bonded to Gr but at the same time also bound to the substrate. However, these atoms needed to be excluded when their sum exceeded five. This is because such situations almost always arose from impacts, which brought a large area of Gr into contact with the substrate. We expect that all such configurations would detach from the substrate upon annealing and, therefore, did not include them in the trapping yield. These cases were almost never encountered at intermediate energies, but instead showed up at the lowest and the highest irradiation energies.

**Conflict of Interest:** The authors declare no competing financial interest.

**Acknowledgment.** J.K. acknowledges financial support from the Austrian Science Fund (FWF) through project M 1481-N20; E.H.Å. and J.K. from the University of Helsinki Funds; and A.V.K. from the Academy of Finland through project No. 263416.

**Supporting Information Available:** The Supporting Information contains spectroscopic measurements of Gr nanoplatelets and defects, an STM annealing series of Xe<sup>+</sup>-irradiated Gr/Ir(111), an STM image demonstrating the interaction of Gr nanoplatelets with Ir step edges, and STM topographs of ion exposure of a partial Gr layer. Additionally, MD movies showing the 0.3 keV He, 0.3 keV Xe, and 5 keV Xe ion irradiation events on Gr/Ir(111) (compare Figure 7) are provided. This material is available free of charge via the Internet at <http://pubs.acs.org>.

## REFERENCES AND NOTES

- Novoselov, K. S.; Geim, A. K.; Morozov, S. V.; Jiang, D.; Zhang, Y.; Dubonos, S. V.; Grigorieva, I. V.; Firsov, A. A. Electric Field Effect in Atomically Thin Carbon Films. *Science* **2004**, *306*, 666–669.
- Geim, A. K.; Grigorieva, I. V. Van der Waals Heterostructures. *Nature* **2013**, *499*, 419–425.
- Butler, S. Z.; Hollen, S. M.; Cao, L.; Cui, Y.; Gupta, J. A.; Gutiérrez, H. R.; Heinz, T. F.; Hong, S. S.; Huang, J.; Ismach, A. F.; *et al.* Progress, Challenges, and Opportunities in Two-Dimensional Materials Beyond Graphene. *ACS Nano* **2013**, *7*, 2898–2926.
- Xu, M.; Liang, T.; Shi, M.; Chen, H. Graphene-Like Two-Dimensional Materials. *Chem. Rev.* **2013**, *113*, 3766–3798.
- Chhowalla, M.; Shin, H. S.; Eda, G.; Li, L.-J.; Loh, K. P.; Zhang, H. The Chemistry of Two-Dimensional Layered Transition Metal Dichalcogenide Nanosheets. *Nat. Chem.* **2013**, *5*, 263–275.
- Krasheninnikov, A. V.; Banhart, F. Engineering of Nanostructured Carbon Materials with Electron or Ion Beams. *Nat. Mater.* **2007**, *6*, 723–733.
- Krasheninnikov, A. V.; Nordlund, K. Ion and Electron Irradiation-Induced Effects in Nanostructured Materials. *J. Appl. Phys.* **2010**, *107*, 071301.
- Tapasztó, L.; Dobrik, G.; Nemes-Incze, P.; Vertes, G.; Lambin, P.; Biró, L. P. Tuning the Electronic Structure of Graphene by Ion Irradiation. *Phys. Rev. B* **2008**, *78*, 233407.
- Ugeda, M. M.; Fernández-Torre, D.; Brihuega, I.; Pou, P.; Martínez-Galera, A. J.; Pérez, R.; Gómez-Rodríguez, J. M. Point Defects on Graphene on Metals. *Phys. Rev. Lett.* **2011**, *107*, 116803.
- Ugeda, M. M.; Brihuega, I.; Hiebel, F.; Mallet, P.; Veullien, J.-Y.; Gómez-Rodríguez, J. M.; Ynduráin, F. Electronic and Structural Characterization of Divacancies in Irradiated Graphene. *Phys. Rev. B* **2012**, *85*, 121402.
- Buchowicz, G.; Stone, P. R.; Robinson, J. T.; Cress, C. D.; Beaman, J. W.; Dubon, O. D. Correlation Between Structure and Electrical Transport in Ion-Irradiated Graphene Grown on Cu Foils. *Appl. Phys. Lett.* **2011**, *98*, 032102.
- Akcöltekin, S.; Bukiowska, H.; Peters, T.; Osmani, O.; Monnet, I.; Alzaher, I.; D'Etat, B. B.; Lebius, H.; Schleberger, M. Unzipping and Folding of Graphene by Swift Heavy Ions. *Appl. Phys. Lett.* **2011**, *98*, 103103.
- Kalbac, M.; Lehtinen, O.; Krasheninnikov, A. V.; Keinonen, J. Ion-Irradiation-Induced Defects in Isotopically-Labeled Two Layered Graphene: Enhanced *in-Situ* Annealing of the Damage. *Adv. Mater.* **2013**, *25*, 1004–1009.
- Standop, S.; Lehtinen, O.; Herbig, C.; Lewes-Malandrakis, G.; Craes, F.; Kotakoski, J.; Michely, T.; Krasheninnikov, A. V.; Busse, C. Ion Impacts on Graphene/Ir(111): Interface Channelling, Vacancy Funnels, and a Nanomesh. *Nano Lett.* **2013**, *13*, 1948–1955.
- Blanc, N.; Jean, F.; Krasheninnikov, A. V.; Renaud, G.; Coraux, J. Strains Induced by Point Defects in Graphene on a Metal. *Phys. Rev. Lett.* **2013**, *111*, 085501.
- Åhlgren, E. H.; Hämäläinen, S. K.; Lehtinen, O.; Liljeröth, P.; Kotakoski, J. Structural Manipulation of the Graphene/Metal Interface with Ar<sup>+</sup> Irradiation. *Phys. Rev. B* **2013**, *88*, 155419.
- N'Diaye, A. T.; Coraux, J.; Plasa, T. N.; Busse, C.; Michely, T. Structure of Epitaxial Graphene on Ir(111). *New J. Phys.* **2008**, *10*, 043033.
- Busse, C.; Lazić, P.; Djemour, R.; Coraux, J.; Gerber, T.; Atodiaresei, N.; Caciuc, V.; Brako, R.; N'Diaye, A. T.; Blügel, S.; *et al.* Graphene on Ir(111): Physisorption with Chemical Modulation. *Phys. Rev. Lett.* **2011**, *107*, 036101.
- Trucano, P.; Chen, R. Structure of Graphite by Neutron Diffraction. *Nature* **1975**, *258*, 136–137.
- Ugeda, M. M.; Brihuega, I.; Guinea, F.; Gómez-Rodríguez, J. M. Missing Atom as a Source of Carbon Magnetism. *Phys. Rev. Lett.* **2010**, *104*, 096804.
- Coraux, J.; N'Diaye, A. T.; Engler, M.; Busse, C.; Wall, D.; Buckanie, N. M.; Meyer zu Heringdorf, F.-J.; van Gastel, R.; Poelsema, B.; Michely, T. Growth of Graphene on Ir(111). *New J. Phys.* **2009**, *11*, 023006.
- Nie, S.; Walter, A. L.; Bartelt, N. C.; Starodub, E.; Bostwick, A.; Rotenberg, E.; McCarty, K. F. Growth from Below: Graphene Bilayers on Ir(111). *ACS Nano* **2011**, *5*, 2298–2306.
- Nieuwenhuys, B. E.; Sachtler, W. M. H. Crystal Face Specificity of Xenon Adsorption on Iridium Field Emitters. *Surf. Sci.* **1974**, *45*, 513–529.
- Gränäs, E.; Knudsen, J.; Schröder, U. A.; Gerber, T.; Busse, C.; Arman, M. A.; Schulte, K.; Andersen, J. N.; Michely, T. Oxygen Intercalation under Graphene on Ir(111): Energetics, Kinetics, and the Role of Graphene Edges. *ACS Nano* **2012**, *6*, 9951–9963.
- Petrović, M.; Šrut Rakić, I.; Runte, S.; Busse, C.; Sadowski, J. T.; Lazić, P.; Pletikosić, I.; Pan, Z.-H.; Milun, M.; Pervan, P.; *et al.* The Mechanism of Caesium Intercalation of Graphene. *Nat. Commun.* **2013**, *4*, 2772.
- Cun, H.; Iannuzzi, M.; Hemmi, A.; Roth, S.; Osterwalder, J.; Greber, T. Immobilizing Individual Atoms beneath a Corrugated Single Layer of Boron Nitride. *Nano Lett.* **2013**, *13*, 2098–2103.
- Cun, H.; Iannuzzi, M.; Hemmi, A.; Osterwalder, J.; Greber, T. Implantation Length and Thermal Stability of Interstitial Ar

- Atoms in Boron Nitride Nanotubes. *ACS Nano* **2014**, *8*, 1014–1021.
28. Gómez Daz, J.; Ding, Y.; Koitz, R.; Seitsonen, A. P.; Iannuzzi, M.; Hutter, J. Hexagonal Boron Nitride on Transition Metal Surfaces. *Theor. Chem. Acc.* **2013**, *132*, 1350.
29. N'Diaye, A. T.; van Gastel, R.; Martnez-Galera, A. J.; Coraux, J.; Hattab, H.; Wall, D.; Meyer zu Heringdorf, F.-J.; Horn-von Hoegen, M.; Gómez-Rodrguez, J. M.; Poelsema, B.; et al. *In Situ* Observation of Stress Relaxation in Epitaxial Graphene. *New J. Phys.* **2009**, *11*, 113056.
30. Hattab, H.; N'Diaye, A. T.; Wall, D.; Klein, C.; Jnawali, G.; Coraux, J.; Busse, C.; van Gastel, R.; Poelsema, B.; Michely, T.; et al. Interplay of Wrinkles, Strain, and Lattice Parameter in Graphene on Iridium. *Nano Lett.* **2012**, *12*, 678–682.
31. Henkelman, G.; Uberuaga, B. P.; Jónsson, H. A Climbing Image Nudged Elastic Band Method for Finding Saddle Points and Minimum Energy Paths. *J. Chem. Phys.* **2000**, *113*, 9901.
32. Riikonen, S.; Krasheninnikov, A. V.; Halonen, L.; Nieminen, R. M. The Role of Stable and Mobile Carbon Adspecies in Copper-Promoted Graphene Growth. *J. Phys. Chem. C* **2012**, *116*, 5802–5809.
33. Michely, T.; Teichert, C. Adatom Yields, Sputtering Yields, and Damage Patterns of Single-Ion Impacts on Pt(111). *Phys. Rev. B* **1994**, *50*, 11156–11166.
34. Petersen, A.; Busse, C.; Polop, C.; Linke, U.; Michely, T. From Erosion to Bombardment-Induced Growth on Ir(111). *Phys. Rev. B* **2003**, *68*, 245410.
35. Lehtinen, O.; Kotakoski, J.; Krasheninnikov, A. V.; Tolvanen, A.; Nordlund, K.; Keinonen, J. Effects of Ion Bombardment on a Two-Dimensional Target: Atomistic Simulations of Graphene Irradiation. *Phys. Rev. B* **2010**, *81*, 153401.
36. Åhlgren, E. H.; Kotakoski, J.; Lehtinen, O.; Krasheninnikov, A. V. Ion Irradiation Tolerance of Graphene as Studied by Atomistic Simulations. *Appl. Phys. Lett.* **2012**, *100*, 233108.
37. Kresse, G.; Furthmüller, J. Efficiency of *Ab-Initio* Total Energy Calculations for Metals and Semiconductors Using a Plane-Wave Basis Set. *Comput. Mater. Sci.* **1996**, *6*, 15–50.
38. Kresse, G.; Furthmüller, J. Efficient Iterative Schemes for *Ab Initio* Total-Energy Calculations Using a Plane-Wave Basis Set. *Phys. Rev. B* **1996**, *54*, 11169–11186.
39. Blöchl, P. E. Projector Augmented-Wave Method. *Phys. Rev. B* **1994**, *50*, 17953–17979.
40. Björkman, T. Van der Waals Density Functional for Solids. *Phys. Rev. B* **2012**, *86*, 165109.
41. Nordlund, K.; Ghaly, M.; Averback, R. S.; Caturla, M.; Diaz de la Rubia, T.; Tarus, J. Defect Production in Collision Cascades in Elemental Semiconductors and fcc Metals. *Phys. Rev. B* **1998**, *57*, 7556–7570.
42. Albe, K.; Nordlund, K.; Averback, R. S. Modeling the Metal-Semiconductor Interaction: Analytical Bond-Order Potential for Platinum-Carbon. *Phys. Rev. B* **2002**, *65*, 195124.
43. Brenner, D. W.; Shenderova, O. A.; Harrison, J. A.; Stuart, S. J.; Ni, B.; Sinnott, S. B. A Second-Generation Reactive Empirical Bond Order (REBO) Potential Energy Expression for Hydrocarbons. *J. Phys.: Condens. Matter* **2002**, *14*, 783–802.
44. Ziegler, J. F.; Biersack, J. P.; Littmark, U. In *Treatise on Heavy-Ion Science*; Bromley, D., Ed.; Springer US: New York, 1985; pp 93–129.
45. Berendsen, H. J. C.; Postma, J. P. M.; van Gunsteren, W. F.; DiNola, A.; Haak, J. R. Molecular Dynamics with Coupling to an External Bath. *J. Chem. Phys.* **1984**, *81*, 3684.